Instantaneous shape sampling: A model for the γ-absorption cross section of transitional nuclei

Bentley, I.; Brant, Slobodan; Donau, F.; Frauendorf, S.; Kampfer, B.; Schwengner, R.; Zhang, S. Q.

Instantaneous shape sampling: A model for the γ-absorption cross section of transitional nuclei

I. Bentley,[1] S. Brant,[2] F. Dönau,[3] S. Frauendorf,[1] B. Kämpfer,[3] R. Schwengner,[3] and S. Q. Zhang[4]

[1]*Department of Physics, University of Notre Dame, Notre Dame, Indiana 46556, USA*

[2]*Department of Physics, Faculty of Science, University of Zagreb, 10000 Zagreb, Croatia*

[3]*Institut für Strahlenphysik, Forschungszentrum Dresden-Rossendorf, 01314 Dresden, Germany*

[4]*School of Physics and State Key Laboratory of Nuclear Physics and Technology, Beijing University, Beijing 100871, People's Republic of China*

The influence of the quadrupole shape fluctuations on the dipole vibrations in transitional nuclei is investigated in the framework of the instantaneous shape sampling model, which combines the interacting boson model for the slow collective quadrupole motion with the random phase approximation for the rapid dipole vibrations. Coupling to the complex background configurations is taken into account by folding the results with a Lorentzian with an energy-dependent width. The low-energy portion of the γ-absorption cross section, which is important for photonuclear processes, is studied for the isotopic series of Kr, Xe, Ba, and Sm. The experimental cross sections are well reproduced. The low-energy cross section is determined by the Landau fragmentation of the dipole strength and its redistribution caused by the shape fluctuations. Collisional damping only wipes out fluctuations of the absorption cross section, generating the smooth energy dependence observed in experiment. In the case of semimagic nuclei, shallow pygmy resonances are found, in agreement with experiment.

I. INTRODUCTION

The cross sections of photonuclear processes, such as (γ, n), (n, γ), (γ, p), (p, γ), (γ, α), and (α, γ), are key elements in various astrophysical scenarios, like supernovae explosions or γ-ray bursts. Precise values of these basic data are also indispensable for simulations of processes of nuclear technology. Many of the relevant reactions involve unstable nuclei for which measurements of the cross sections are not possible. Therefore, the cross sections have to be taken from theory. In many cases the statistical Hauser-Feshbach model is applicable, which decomposes the total reaction cross section into a product of the absorption and emission probabilities of the particles and γ quanta. Theoretical models that predict the dipole strength function for γ absorption or emission through the whole nuclear chart are therefore of utmost importance. The reactions take place in an energy interval of a few MeV around the particle-emission thresholds. Aside from the mentioned applications in nuclear astrophysics and nuclear technology, the understanding of the mechanisms that determine the structure of the dipole strength function on the low-energy tail of the isovector giant dipole resonance is a challenge of its own to nuclear theory.

The present article proposes and tests a new approach, which we call instantaneous shape sampling (ISS). This approach combines the microscopic quasiparticle random phase approximation for dipole excitations with the phenomenological interacting boson approximation for a dynamical treatment of the nuclear shape. The ISS approach aims at the microscopic description of the dipole strength function of the many transitional nuclei ranging between the regions of spherical and well-deformed shapes, which execute large shape fluctuations. The special focus of our calculations is the behavior of dipole strength in the energy range of a few MeV around the particle-emission threshold. These energies are most important for the applications mentioned. It is also

the range where there are great gaps in theoretical and experimental knowledge about the dipole strength function. ISS was suggested in Ref. [1], where it was applied to the Mo, Zr, and Sr isotopes. Further, it was applied to ^{139}La [2]. The present work describes the model in detail and presents additional results of systematic calculations in various regions of the nuclear chart. Our paper is organized as follows. In Sec. II, basic features of the photonuclear absorption cross section are recalled. The ISS model is introduced in Sec. III. Section IV presents the calculational scheme of ISS. The version of the quasiparticle random phase approximation used in this paper is laid out in Sec. V. Section VI contains the detailed discussion of our results. The range of validity of our ISS approach is discussed in Sec. VII. Conclusions are drawn in Sec. VIII.

II. THE ABSORPTION CROSS SECTION

The cross section $\sigma_{E1}(E)$ for the absorbtion of electric dipole ($E1$) radiation at the energy E by an even-mass nucleus is

$$\sigma_{E1}(E) = 4.022 E S_{E1}(E), \quad S_{E1}(E) = \frac{dB(E1; E) \uparrow}{dE}, \quad (1)$$

where the strength function $S_{E1}(E)$ is the derivative of the reduced transition probability $B(E1; E) \uparrow$ for a transition from the 0^+ ground state to a 1^- excited state at energy E. The units in Eq. (1) are E in MeV, σ_{E1} in mb, and $B(E1)$ in e^2 fm^2. For magnetic dipole ($M1$) radiation one has

$$\sigma_{M1}(E) = 0.0452 E S_{M1}(E), \quad S_{M1}(E) = \frac{dB(M1; E) \uparrow}{dE}, \quad (2)$$

where the strength function $S_{M1}(E)$ is the derivative of the reduced transition probability $B(M1; E) \uparrow$ for a transition from the 0^+ ground state to a 1^+ excited state at energy E. The units in Eq. (2) are E in MeV, σ_{M1} in mb, and $B(M1)$ in μ_N^2. The absorption cross section enters directly the total

cross section for (γ, particle) reactions. For the (particle, γ) reactions, the dipole strength function determines the γ cascade depopulating excited states. We present only results for the absorption cross sections, because the strength function can be easily obtained from the absorption cross sections by means of Eqs. (1) and (2).

The $E1$ part of the absorption cross section dominates in the energy range above 6 MeV, where the $M1$ part amounts to only a few percent of the total cross section (see Sec. V). Thus, in reviewing previous work we focus on the electric part. The prominent structure of the cross section $\sigma_{E1}(E)$ is the giant dipole resonance (GDR). It can be approximated by a Lorentzian [3,4]

$$\sigma(E, \Gamma) = \sigma_R \frac{(\Gamma E)^2}{\left(E^2 - E_R^2\right)^2 + (E\Gamma)^2} \qquad (3)$$

and is determined by three parameters, the resonance energy E_R, the maximum height σ_R, and the width Γ. This expression represents the amount of radiation absorbed by a classical damped dipole oscillator, where $\Gamma/\hbar$ is the dissipation rate of the vibrational energy, which determines the width of the resonance. Concerning the low-energy tail, the question arises as to whether and in what way Γ depends on the energy. The authors of Ref. [5] suggest $\Gamma \propto E_x^2$ based on the theory of Fermi liquids, where E_x is the photon energy. Other authors consider the width as constant. For axially deformed nuclei, the GDR splits into two peaks [6,7] and for triaxial deformation into three peaks, where each of the modes can be described by a Lorentzian [8]. The different resonance frequencies reflect the different wavelengths along the principal axes of the deformed nucleus [4]. The Hauser-Feshbach codes, used to calculate reaction rates for various applications, such as the one in Ref. [9], traditionally employ some version of the two-Lorentzian model [10]. The deformation parameters of the assumed axial shape are taken either from experimental $B(E2)$ values or from calculations by means of the micro-macro (MM) method [11,12].

In Ref. [8] the experimental absorption cross section was analyzed in terms of a model of three individual Lorentzians with relative resonance energies related to the nuclear deformation according to hydrodynamics (see, e.g., Ref. [4]) and $\Gamma \propto E_R^{1.6}$, where E_R is the energy of the resonance. Recently, cross sections in the GDR region were combined with novel photon-scattering data obtained from experiments at the ELBE accelerator [13–17], which provided for the first time cross sections from the low-energy region up to the GDR region. The new data suggest that the smooth Lorentzian extrapolation to energies far below the peak region of the GDR provides a rough estimate for the average trend of the cross sections, but is not capable of describing resonance phenomena observed in this energy region. Although the experimental information about the cross section below the particle-emission threshold is still sparse, there is evidence for pronounced fluctuations and resonancelike structures that are above the Lorentzian [13,15,16]. Furthermore, below 5 MeV the cross section changes more and more into a discrete spectrum of individual $1^{\pm}$ states. This energy region becomes important in reactions involving neutron-rich nuclei. The dipole strength function

that determines the γ cascade in (particle, γ) reactions may also belong to this energy region if the Q value is low.

A more microscopic approach is needed to account for these shortcomings. Moreover, a microscopically founded description of the dipole strength function is a long-standing challenge of its own to nuclear theory. The traditional approach is to start from the quasiparticle random phase approximation (QRPA) [18], which extends the mean field description of the nucleus by taking into account the quasibosonic part of the residual interaction, which generates a coupling between the elementary two-quasiparticle excitations in the self-consistent mean field potential [19]. After the QRPA dispersion relation is solved, one obtains a discrete series of states that are superpositions of the two-quasiparticle excitations. These states describe how the cross section of the collective dipole vibration is spread over the two-quasiparticle excitations. This mechanism is called Landau fragmentation (or Landau damping in the case of a dense two-quasiparticle spectrum). It accounts for a part of the width of the GDR.

For example, in Fig. 1, we show the absorption cross section for the axially deformed nucleus ^{130}Ba. The discrete energies of the QRPA solutions are folded with a Breit-Wigner distribution with a width of $\Gamma = 0.1$ MeV [see Eq. (4) below]. The strong fluctuations of the cross section reflect the individual structure of the two-quasiparticle excitations that contribute to the GDR. The nucleus is prolate. The two main peaks correspond to the vibrations along the long axis ($K = 0$, low) and along the short axis ($|K| = 1$, high). The Landau fragmentation generates a cross section σ at low energy, which, as discussed in the following, is of the order of the observed one. However, there must be strong additional couplings of the QRPA "doorway" states to more complicated excitations, which smooth out the fluctuations completely.

In standard QRPA calculations, these couplings are taken into account in a phenomenological way by folding the QRPA solutions with a Breit-Wigner or Lorentz function, analogously to the three solutions of the dipole oscillator just mentioned. We prefer for simplicity the Breit-Wigner distribution, which is practically equivalent to the Lorentz function used in Eq. (3). The Breit-Wigner distribution is given by

$$\sigma_{\text{QRPA}}(E, \Gamma) = \sum_\nu \sigma_\nu \frac{\Gamma/2\pi}{(E_\nu - E)^2 + \Gamma^2/4}, \qquad (4)$$
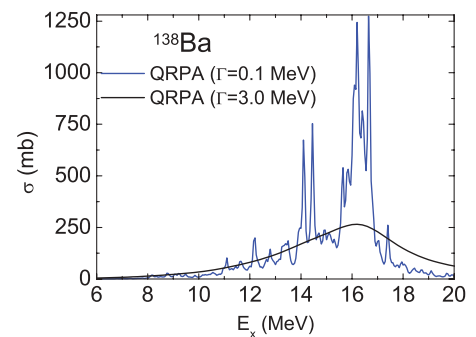

FIG. 1. (Color online) Absorption cross section of ^{130}Ba calculated in the QRPA with the equilibrium deformation $\beta = 0.171$ (cf. Table II). Solid black curve, width $\Gamma = 3$ MeV; thin blue curve, width $\Gamma = 0.1$ MeV.

where σ_ν is the cross section of the QRPA solution at the energy E_ν. The cross section takes on the smooth shape seen in experiments, if folded with a large width $\Gamma = 3$ MeV. In the considered case the relation $E_R(K = 1) - E_R(K = 0) < \Gamma$ holds, and the two peaks merge into a broad peak, the large width of which reflects the deformation. QRPA calculations for static spherical or deformed shapes (see, e.g., Refs. [20–22]) use such a smoothing procedure to account phenomenologically for the neglected coupling to more complex configurations. Accordingly, in Refs. [23,24] strength functions for applications in Hauser-Feshbach codes were calculated throughout the nuclear chart. The authors start from the Skyrme Hartree-Fock-Bogoliubov mean field, which provides the deformation parameters. However, they carry out the QRPA calculations for spherical shapes only and include the splitting caused by deformation in a phenomenological way. Hence, the QRPA describes the parts of the GDR width that originate from Landau fragmentation and static deformation.

The microscopic origin of the remaining part of the spreading of the GDR has been reviewed, for example, in Refs. [25,26]. The escape width $\Gamma_\uparrow$ accounts for the emission of particles from the QRPA states. It is only of importance for light nuclei or nuclei near the drip lines. The spreading width $\Gamma_\downarrow$ describes the coupling to more complex configurations. It is suggested that the coupling to correlated four-quasiparticle states should contribute to $\Gamma_\downarrow$, whereas the coupling to six-quasiparticle and higher-order quasiparticle excitations will only wash out some residual fluctuations of the strength function. For spherical nuclei, the coupling to the four-quasiparticle configurations has been taken into account in the framework of the quasiparticle-phonon models, such as [20–34]. The resulting strength functions reproduce the spreading of the GDR. Although a generalization to nuclei with static deformation is possible [20], calculations have been restricted to spherical nuclei so far because of the substantial increase of the numerical work. However, the principal problems arise in transitional nuclei that undergo large-amplitude shape fluctuations.

III. THE ISS MODEL

In the following we suggest an alternative approach. We explicitly describe the coupling of the dipole vibration to the two-quasiparticle excitations by means of the QRPA for deformed shapes. Out of the couplings of these QRPA doorway states to the more complex configurations, we take into account only the low-energy collective quadrupole excitations, which represent the softest mode that couples most strongly to the dipole mode. The quadrupole mode is described by a model that allows for large-amplitude motion, i.e., one that is suited for transitional nuclei, which are the main object of our work. The typical frequencies $\hbar\omega(2^+)$ of *collective* quadrupole excitations are smaller than 1 MeV, which means about a factor of 10 less than the energies $\hbar\omega(1^-)$ of the dipole excitations. Because the quadrupole motion is much slower than the dipole one we use the adiabatic approximation: By means of

the QRPA, we calculate the dipole absorption cross section $\sigma_{E1,M1}(E, \beta_n, \gamma_n)$ for a set of instantaneous deformation parameters (β_n, γ_n) of the mean field. We determine the probability $P(\beta_n, \gamma_n)$ of each shape being present in the ground state and obtain the total cross section as the incoherent sum of the instantaneous ones,

$$\sigma_{\text{ISS}}(E) = \sum_n P(\beta_n, \gamma_n)[\sigma_{E1}(E, \beta_n, \gamma_n) + \sigma_{M1}(E, \beta_n, \gamma_n)]. \quad (5)$$

The zero-point motion in the ground state with respect to the collective quadrupole modes is represented by the set of instantaneous shapes (β_n, γ_n) and their probabilities $P(\beta_n, \gamma_n)$. As a first step, the "dynamical" ground state is constructed in the framework of the interacting boson approximation (IBA) [35]. The IBA is not a compulsory choice. Other approaches that describe large-amplitude quadrupole motion could be used as well. However, the IBA treats the large-amplitude quadrupole motion in an efficient way and has proven to be successful for a systematic description of transitional nuclei. In practice it is very easy to handle because it has a minimum set of free parameters. Moreover, it allows us to generate the discrete set of instantaneous shapes (β_n, γ_n) and the probabilities $P(\beta_n, \gamma_n)$ in a simple way. In the next step, a series of QRPA calculations is performed, where (β_n, γ_n) defines the shape of the Woods-Saxon (WS) potential in the QRPA Hamiltonian. Then the total cross section is obtained as the incoherent sum Eq. (5) of the respective cross sections $\sigma_{E1}(E, \beta_n, \gamma_n)$ and $\sigma_{M1}(E, \beta_n, \gamma_n)$ multiplied by the probabilities $P(\beta_n, \gamma_n)$. Finally, the coupling to the more complex configurations is taken into account by folding $\sigma_{\text{ISS}}(E)$ with the Breit-Wigner function,

$$\sigma_{\text{ISS+CD}}(E) = \int dE' \sigma_{\text{ISS}}(E') \frac{\Gamma(E')/2\pi}{(E - E')^2 + \Gamma(E')^2/4}. \quad (6)$$

The width is chosen to depend quadratically on the photon energy E as expected for collisional damping (CD), i.e., $\Gamma(E) = \alpha E^2$ [5,25,26]. We will refer to this phenomenological correction as "collisional damping" (ISS + CD) although it comprises all kinds of couplings that are not explicitly taken into account. The value $\alpha = 0.0111$ used in our calculations corresponds to $\Gamma(E) = 2.5$ MeV at $E = 15$ MeV. The relation $\hbar\omega(2^+)/\hbar\omega(1^-) \ll 1$ is taken as a justification for neglecting possible phase correlations between the different shapes (β_n, γ_n). In other words, we assume that the deformation does not change during the excitation of the nucleus by the absorbed photons, that is, the photon "sees" the shape of the nucleus that absorbs it. Thus, the photon current on a target samples the various instantaneous shapes of the nuclei in the ground state. Accordingly we suggest the name instantaneous shape sampling (ISS) QRPA for the approach. In the following the different steps of the ISS-QRPA approach are explained in more detail, results of calculations for a selection of nuclei are presented, and a more sophisticated justification of the ISS procedure is given.

IV. THE CALCULATION OF THE INSTANTANEOUS SHAPES AND PROBABILITIES WITHIN THE IBA

The family of collective quadrupole states in transitional nuclei is described by the simplified IBA Hamiltonian suggested in Refs. [36,37],

$$H_{\text{IBA}} = c \left[(1 - \zeta) \hat{n}_d - \frac{\zeta}{4N_b} \, Q \cdot Q \right], \tag{7}$$

$$Q_\mu = s^\dagger d_\mu + d_\mu^\dagger s + \chi \, [d^\dagger \otimes d]_{2\mu}. \tag{8}$$

The operators $s^\dagger$, s and $d_\mu^\dagger$, d_μ denote the $l = 0$ and $l = 2$ boson operators, respectively, of the IBA-1 model [35], and $\hat{n}_d$ is the number operator of d bosons. The factor c sets the energy scale and has no influence on the structure of the states. The isoscalar quadrupole operator Q_μ appearing in the Hamiltonian is also used to define the electric quadrupole ($E2$) transition operator

$$T_\mu(E2) = e_b Q_\mu, \tag{9}$$

where e_b represents the boson effective charge in units of e b. In IBA applications the total number N_b of s and d bosons is usually chosen to be half of the number of valence particles or holes relative to the nearest closed shells in the considered nucleus. In contrast, we fix the value to $N_b = 10$. The reason is that N_b determines the number of instantaneous shapes to be sampled. The small values of N_b near closed shells would not allow us to represent the fluctuations of the shape of these nuclei. Fitting the IBA parameters, we found that we could reproduce the low-energy states with the same accuracy as for the traditional IBA choice of N_b. The range of the essential parameters ζ and χ in Eqs. (7) and (8) is restricted to the intervals $[0,1]$ and $[0, -\sqrt{7}/2]$, repecively. Within this range, which defines the so-called symmetry triangle shown in Fig. 2, the whole variety of transitional structures between the vibrational, rotational, and γ-independent nuclei is included. For a given nucleus the values of ζ and χ are searched for by a fit to the experimental energy ratios $E(4_1)/E(2_1)$, $E(0_2)/E(2_1)$, and $E(2_2)/E(2_1)$. The resulting IBA parameter values (ζ, χ) for the nuclides considered in this paper are
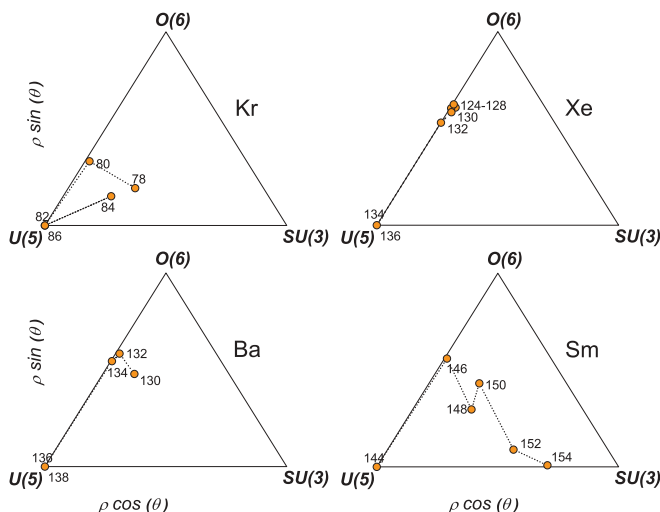
TABLE I. Optimal IBA parameters ζ, χ and the boson charge e_b for the considered nuclides.

A	N	ζ	χ	e_b (e b)
		Kr		
78	42	0.47	−0.79	0.088
80	44	0.35	−0.06	0.075
82	46	0.0	−1.2	0.067
84	48	0.35	−0.76	0.044
86	50	0.0	−1.2	0.049
		Xe		
124	70	0.63	−0.04	0.094
126	72	0.61	−0.01	0.086
128	74	0.63	−0.01	0.083
130	76	0.60	−0.03	0.079
132	78	0.53	−0.0	0.074
134	80	0.0	−1.20	0.082
136	82	0.0	−1.20	0.085
		Ba		
130	74	0.61	−0.26	0.105
132	76	0.60	−0.03	0.091
134	78	0.55	−0.01	0.084
136	80	0.0	−1.20	0.091
138	82	0.0	−1.20	0.068
		Sm		
144	82	0.0	−1.20	0.072
146	84	0.57	−0.02	0.071
148	86	0.54	−0.59	0.087
150	88	0.64	−0.41	0.108
152	90	0.62	−1.15	0.146
154	92	0.71	−1.31	0.142

collected in Table I. Figure 2 places the values for the Kr, Xe, Ba, and Sm isotopes into the symmetry triangles, where the definition of the polar coordinates (ρ, θ) according to Ref. [37] is applied. Such contour lines within the symmetry triangle may help in extrapolation to nuclei with less well-known excitation spectra.

The next step is the calculation of the probability distribution $P(\beta_n, \gamma_n)$ of the deformations β_n and γ_n in the 0^+ ground state of the boson Hamiltonian Eq. (7). We follow the method proposed in Refs. [38,39]. We relate the IBA to the shape of the Woods-Saxon potential used in the QRPA by assuming that its deformation parameters β, γ are the same as in the expression for the electric quadrupole ($E2$) transition operator of a charged liquid drop,

$$T_\mu(E2) = \frac{3ZeR^2}{4\pi} \beta \left[D_{\mu 0}^2 \cos \gamma + \left(D_{\mu 2}^2 + D_{\mu -2}^2 \right) \frac{\sin \gamma}{\sqrt{2}} \right], \tag{10}$$

where the $D_{\mu \nu}^2$ functions transform the quadrupole moments from the body-fixed frame to the laboratory frame in the standard way. From Eqs. (9) and (10) it follows that the two scalar invariants constructed from the IBA quadrupole operator Q_μ given by Eq. (8) are connected to the deformation

FIG. 2. (Color online) IBA symmetry triangles for the even-A isotopic chains $^{78-86}$Kr, $^{124-136}$Xe, $^{130-138}$Ba, and $^{144--154}$Sm.

as follows:

$$\hat{q}_2 = [Q \otimes Q]_0 \propto \beta^2, \tag{11}$$

$$\hat{q}_3 = [Q \otimes [Q \otimes Q]_2]_0 \propto \beta^3 \cos 3\gamma. \tag{12}$$

A set of localized states $|n\rangle$ is generated by diagonalizing $\hat{q}_2$ and $\hat{q}_3$ within the basis of $N_b = 10$ of s-d boson states. Because the scalars $\hat{q}_2$ and $\hat{q}_3$ commute, they can be simultaneously diagonalized. As we are interested only in the probability distribution $P(\beta_n, \gamma_n)$ of the IBA ground state $|0_1^+\rangle$, the diagonalization is restricted to the set of 0^+ basis states within the boson space of maximal $N_b = 10$ d bosons. The eigenvalues $q_{2,n}$ and $q_{3,n}$ provide the values of the deformation parameters (β_n, γ_n) that are assigned to each localized state $|n\rangle$ by the relations

$$\beta_n^2 = \sqrt{5}\left(\frac{4\pi e_b}{3ZeR^2}\right)^2 q_{2,n}, \quad \cos 3\gamma_n = \sqrt{\frac{7}{2\sqrt{5}}}\frac{q_{3,n}}{(q_{2,n})^{3/2}}, \tag{13}$$

where e_b is the effective boson charge and $R = 1.2\,A^{1/3}$ fm is the nuclear charge radius [cf. Eqs. (9) and (10)]. The eigenstates $|n\rangle$ of the operators (11), (12) are identified with "instantaneous" mean field states with the deformation parameters (β_n, γ_n). As usual, the boson charge e_b is adjusted to measured $B(E2, 2_1^+ \to 0_1^+)$ values [35], which are taken from the compilation [40]. The probabilities $P(\beta_n, \gamma_n)$ are finally obtained by projecting the eigenstates $|n\rangle$ onto the IBA ground $|0^+\rangle$, i.e.,

$$P(\beta_n, \gamma_n) = |\langle 0_1^+|n\rangle|^2. \tag{14}$$

Our procedure assumes that the instantaneous charge density and the instantaneous mean field have the same deformation.

As an example, we discuss the IBA part of the ISS calculations for the even-A chain $^{78-86}$Kr. In the top part of Table I the IBA parameters (ζ, χ) are given, and in Fig. 3 the resulting instantaneous deformations (β_n, γ_n) and the probabilities P_n are displayed. Note that (β, γ) are curvilinear coordinates with the volume element $d\beta\beta^4 d\gamma \sin 3\gamma$. These geometric factors are part of the probabilities P_n. This has the
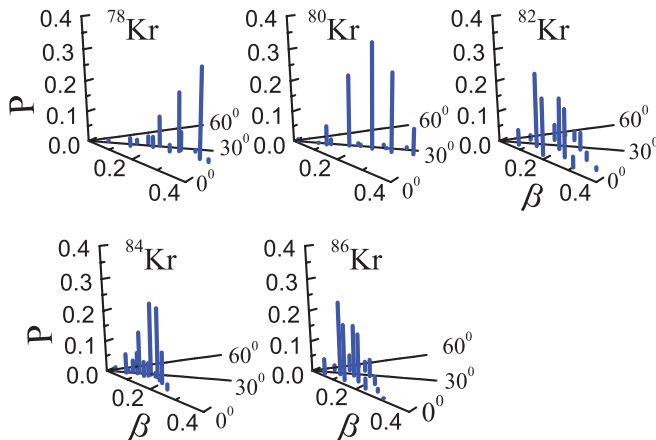
consequence that $\gamma = 30°$ is favored. For example, ^{80}Kr has $\chi \approx 0$, which means that it tends to a γ instabliblity between the U(5) and O(6) limits (cf. Fig. 2). The corresponding distribution in Fig. 3 looks as if the nucleus had a stable triaxial deformation, which, however, only reflects the factor $\sin 3\gamma$ in the volume element. In a similar fashion, $\beta = 0$ is suppressed. For example, ^{86}Kr has $\zeta = 0$, which means it is a spherical vibrator [U(5) limit]. The corresponding distribution in Fig. 3 looks as if the nucleus had a stable deformation, which, however, only reflects the factor β^4 in the volume element.

V. THE QRPA

The Hamiltonian H for the QRPA [19] comprises the mean field part $h_{\rm mf}$ and a residual dipole-dipole interaction $v_{\rm res}$,

$$H = h_{\rm mf}^{(p)}(\beta_n, \gamma_n) + h_{\rm mf}^{(n)}(\beta_n, \gamma_n) + v_{\rm res},$$

$$h_{\rm mf}^{(\tau)}(\beta_n, \gamma_n) = h_{\rm WS}^{(\tau)}(\beta_n, \gamma_n) + \Delta^{(\tau)}(P^{+(\tau)} + P^{(\tau)}) - \lambda^{(\tau)}N^{(\tau)}, \tag{15}$$

where the indices $\tau = p, n$ refer to protons and neutrons, respectively. The spatial part of the mean field $h_{\rm WS}^{(\tau)}(\beta_n, \gamma_n)$ is the triaxial Woods-Saxon potential (for parameters see Ref. [41]). The deformation parameters (β_n, γ_n) of the WS potential define the instantaneous quadrupole-deformed shape about which the nucleus executes the isovector dipole oscillations. In order to describe the partial occupancies of the single-particle levels in open-shell nuclei, a static monopole pair potential is added to the WS part in Eq. (15); it is defined by the gap parameter $\Delta^{(\tau)}$ and the Fermi energy $\lambda^{(\tau)}$. Therein, $N^{(\tau)}$ and $P^{(\tau)+}$ denote the particle number and monopole pairing operators for the protons and neutrons, respectively.

The residual interaction consists of two terms, $v_{\rm res} = v_{\rm res}^{(E1)} + v_{\rm res}^{(M1)}$, where the index $E1$ refers to the negative-parity electric excitations and the index $M1$ to the positive-parity magnetic excitations. The $E1$ and the $M1$ dipole excitations of the QRPA are calculated separately, and their contributions to transition strengths are added up. Our QRPA calculations assume schematic interactions of the dipole-dipole type. The $E1$ part is given by the electric dipole-dipole interaction

$$v_{\rm res}^{(E1)} = \frac{1}{2}\varkappa_{t=0}\left(\sum_{i=1,A}\vec{x}_i''\right)^2 + \frac{1}{2}\varkappa_{t=1}\left(\sum_{i=1,A}\tau_i\vec{x}_i''\right)^2, \tag{16}$$

where here $\tau = \pm 1$ holds for neutrons and protons, respectively. The interaction $v_{\rm res}^{(E1)}$ is expressed in terms of the doubly stretched coordinates $\vec{x}''$ referring to the nuclear self-consistency model [42]. The term $v_{res}^{(E1)}$ is the simplest ansatz for a residual interaction with the signature 1^-. The inclusion of an octupole-octupole term has been investigated too. It is not taken into account here, because it was found that it had practically no effect on the $E1$ cross section. It is worth mentioning that, according to the investigations [22,43], the isovector dipole term is the most important contribution in an expansion of a realistic Skyrme-type interaction into separable interaction terms. As suggested in Ref. [44], the isoscalar ($t = 0$) interaction term is used for removing the spurious center-of-mass motion. Choosing a value $\varkappa_{t=0} = 1000$ MeV fm^{-2} for the isoscalar coupling constant ensures

FIG. 3. (Color online) Probability distributions for $^{78-86}$Kr. The instantaneous nuclear shapes over the β-γ plane were found by means of the IBA with the parameters given in Table I.

that the QRPA states have no spurious contributions. The isovector strength constant $\varkappa_{t=1}$ determines the mean position of the GDR. The A dependence of the isovector strength $\varkappa_{t=1}$ is assumed to be given by the self-consistent strength factor [42]

$$\varkappa_{t=1} = -\varkappa_{\text{sc}}\,\eta = -\frac{M\omega_o^2}{A}\,\eta, \tag{17}$$

where M is the nucleon mass and $\hbar\omega_o = 41A^{1/3}$ MeV. For the remaining factor η an empirical value $\eta \approx 3$ fm^{-2} is estimated from the systematics of the GDR peak energy. In our QRPA calculations, the η value is kept constant within an isotopic chain and is adjusted to the empirical peak position of the GDR of one of the isotopes in each chain.

Our simple dipole-dipole interaction (16) is not consistent with the WS potential. Therefore, the center-of-mass mode does not appear as a spurious zero-energy QRPA solution, which decouples from the physical solutions. Giving the isoscalar term a large strength "freezes" the center-of-mass motion in each spatial direction, i.e., the corresponding spurious pole is shifted to high energy, such that it is practically decoupled from the QRPA solutions in the considered energy region. Such a choice of the interaction does not account for possible isoscalar dipole correlations which may generate a *collective* pygmy resonance. (Of course, *noncollective* pygmy resonances of the two-quasiparticle type may still appear, as discussed below.) A more sophisticated interaction would be needed to account for such correlations, which brings back the problem of decoupling the spurious center-of-mass motion. Since the photoexcitation is determined by the isovector dipole operator, isoscalar correlations would play only an indirect role via coupling between the isovector and isoscalar modes. Since the decoupling of the center-of-mass motion is vital to the calculation of the isovector strength function at low energy, we decided to guarantee this by our choice of the isoscalar dipole-dipole interaction. A more sophisticated interaction, which has to be consistent with the deformed mean field, is beyond the scope of this paper, which focuses on the consequences of shape fluctuations. The analogous argument applies to the magnetic interaction terms introduced below. The $M1$ part of the residual interaction v_{res} is the magnetic dipole-dipole interaction

$$v_{\text{res}}^{(M1)} = -\frac{1}{2}\sum_{t=0,1}\kappa_j^t \mathbf{J}^t \cdot \mathbf{J}^t - \frac{1}{2}\sum_{t=0,1}\kappa_s^t \mathbf{S}^t \cdot \mathbf{S}^t. \tag{18}$$

The terms $\mathbf{J}^t \cdot \mathbf{J}^t$ and $\mathbf{S}^t \cdot \mathbf{S}^t$ are composed of the isoscalar ($t = 0$) and isovector ($t = 1$) parts of the total angular momentum operator $\mathbf{J} = \mathbf{L} + \mathbf{S}$ and the spin operator $\mathbf{S}$, i.e., $\mathbf{J}^{t=0,1} = \mathbf{J}^{(p)} + (-1)^t\mathbf{J}^{(n)}$ and $\mathbf{S}^{t=0,1} = \mathbf{S}^{(p)} + (-1)^t\mathbf{S}^{(n)}$. A possible quadrupole-quadrupole interaction term turned out to be unimportant for the $M1$ strength above 4 MeV excitation energy. The same magnetic dipole interaction as in Eq. (18) was used in Ref. [45] to describe the $M1$ properties of the Mo isotopes. In these investigations it turned out that the $M1$ transition strength in the interesting energy region above 5 MeV is completely dominated by spin vibrations that are generated by the strong repulsive isovector spin-spin term $\mathbf{S}^{t=1} \cdot \mathbf{S}^{t=1}$ in Eq. (18). The related strength parameter $\kappa_s^{t=1}$ is not well known from literature. Therefore, we have

used the same value $\kappa_s^{t=1} = -1$ MeV/$\hbar^2$ as in our previous study [45]. The isoscalar spin-spin term $\mathbf{S}^{t=0} \cdot \mathbf{S}^{t=0}$ is neglected because the isoscalar spin part $\mathbf{S}^{t=0}$ in the $M1$ transition operator is reduced by about a factor of 20 as compared to the corresponding isovector spin part. However, a large isoscalar term $\mathbf{J}^{t=0} \cdot \mathbf{J}^{t=0}$ is included by choosing $\kappa_j^{t=0} = 1000$ MeV/$\hbar^2$ in order to eliminate effects of the spurious rotational motion. The isovector term $\mathbf{J}^{t=1} \cdot \mathbf{J}^{t=1}$ is left out because it only influences the scissor mode in deformed nuclei, the $M1$ strength of which appears below 5 MeV [45]. This energy region is not considered in the present work.

The $M1$ strength is essentially generated by spin-flip transitions between high-j spin-orbit partners. Accordingly, it is expected to produce a summed $B(M1)$ strength of a few μ_N^2 distributed in the energy region 7–9 MeV in medium-mass nuclei (see, e.g., [46]). This corresponds to a cross-section contribution of a few millibarns. In some cases this value can reach up to 20% of the corresponding $E1$ cross section in the low-energy region. As an example, we present the QRPA result for the nuclide ^{138}Ba in Fig. 4, showing the $E1$ and $M1$ contributions separately. Because the measurement of the parity is a quite challenging task, there are hitherto only a few experiments that identify the $M1$ part of the dipole strength. For this reason we do not display the relatively small $M1$ contribution to the dipole cross section separately.

Carrying out the QRPA begins with the diagonalization of the deformed WS potential of the Hamiltonian (15) where we use an oscillator basis with the shells $N = 0$–8. The pair field in Eq. (15) is included in the BCS approximation, which transforms the creation and annihilation operators $c_k^\dagger$ and c_k of the WS levels k to the quasiparticle operators

$$a_k^\dagger = u_k c_k^\dagger + v_k c_{\bar{k}}. \tag{19}$$

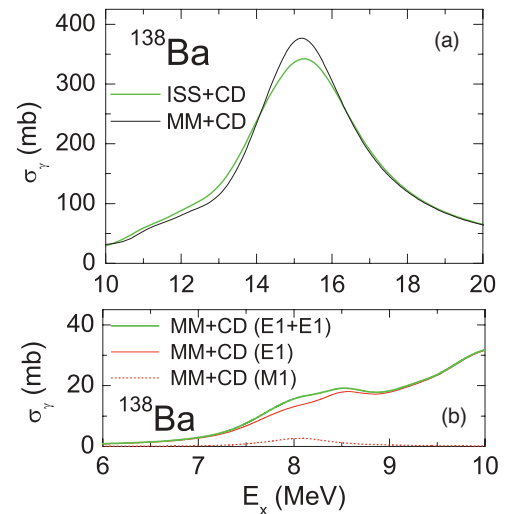FIG. 4. (Color online) Photoabsorption cross section of ^{138}Ba calculated with the ISS-QRPA and energy-dependent width $\Gamma(E_x) = 2.5(E_x/15)^2$ MeV. (b) $E_x = 6$–10 MeV. Red solid curve, $E1$ contribution; red dotted curve, $M1$ contribution; solid green curve, summed $E1 + M1$ cross section. (a) $E_x = 10$–20 MeV. Black curve, QRPA with the equilibrium deformation in Table II; green curve, ISS-QRPA.

Here, u_k and v_k are the usual BCS amplitudes, and $\bar{k}$ labels the time-conjugate WS levels. In terms of the quasiparticle operators the mean field part of the Hamiltonian Eq. (15) takes the diagonal form

$$h_{\mathrm{mf}} = \sum_k \varepsilon_k(a_k^\dagger a_k + a_{\bar{k}}^\dagger a_{\bar{k}}), \tag{20}$$

where $\varepsilon_k = \sqrt{(e_k - \lambda)^2 + \Delta^2}$ are the quasiparticle energies in the WS potential. The values of the pairing gaps $\Delta^{(p,n)}$ are derived from the binding energies by using a five-point formula.

The standard way of performing the QRPA consists of solving the equation of motion

$$[H, \Omega_\nu^\dagger]_{\mathrm{QRPA}} = E_\nu \Omega_\nu^\dagger \tag{21}$$

for the phonon operators $\Omega_\nu^\dagger$ [cf. Eq. (22) below] via a matrix diagonalization [18]. The subscript QRPA in Eq. (21) indicates that only the quasibosonic part of the residual interaction v_{res} is included in the commutator. The set of eigenvalues E_ν forms the discrete spectrum of the vibrational dipole excitations. The eigenvectors of the Hamiltonian in Eq. (21) define the QRPA amplitudes $\phi_{kk'}^{(\nu)}$ and $\psi_{kk'}^{(\nu)}$. The phonon operators,

$$\Omega_\nu^\dagger = \sum_{kk'} \left[\phi_{kk'}^{(\nu)} a_k^\dagger a_{k'}^\dagger + \psi_{kk'}^{(\nu)} a_{k'} a_k \right], \tag{22}$$

create the vibrational states ν as a superposition of two-quasiparticle and two-quasihole excitations. The partial cross section σ_ν for a dipole excitation from the QRPA ground state $|\rangle$ to a vibrational state $|\Omega_\nu^\dagger\rangle$ at the energy E_ν is

$$\sigma_\nu(E) = f^{(\pm)} E_\nu |\langle \Omega_\nu \mathsf{M}_{\mathrm{dipole}}^{(\pm)} \rangle|^2 \delta(E - E_\nu), \tag{23}$$

where $\mathsf{M}_{\mathrm{dipole}}^{(\pm)}$ means the electric $(-)$ or magnetic $(+)$ dipole transition operator. Measuring the cross section in mb and the energies in MeV, the respective scale factors are $f^{(-)} = 4.022/(e^2\,\mathrm{fm}^2)$ and $f^{(+)} = 0.0452/(\mu_N^2)$ [cf. Eqs. (1) and (2)]. The total cross section $\sigma(E)$ is given by summing over all the partial cross sections σ_ν. Finally, we replace $\delta(E - E_\nu)$ by a Breit-Wigner distribution of finite width Γ, which gives the previous expression Eq. (4) for the cross section $\sigma(E, \Gamma)$.

To circumvent the direct evaluation of the equation of motion (21), which involves typically a large matrix diagonalization with a rank of $n \approx 10^4\text{--}10^5$, we apply the strength function method [20]. With this method, the summation in Eq. (4) can be written in terms of a contour integral which finally is cast in an analytical formula for the function $\sigma_{\mathrm{QRPA}}(E, \Gamma)$ that is explicitly given in Ref. [20]. The use of the analytical expression for $\sigma_{\mathrm{QRPA}}(E, \Gamma)$ leads to an enormous simplification of the practical performance of the QRPA which is of crucial importance for taking account of the variety of shapes (β, γ) inherent to the ISS calculations. The QRPA calculations are carried out with a constant width of $\Gamma = 0.1$ MeV. This width is small enough to retain all relevant structure of the cross section. The method is also efficient for a separable interaction that contains more terms than the leading dipole-dipole term considered in our paper. The authors of Ref. [43] demonstrated that such separable interactions well approximated the nonseparable interactions of the Skyrme type.

VI. RESULTS

The results of ISS calculations for the isotopic chains $^{78\text{--}86}$Kr, $^{124\text{--}134}$Xe, $^{128\text{--}134}$Ba, and $^{144\text{--}154}$Sm are shown in Figs. 5–7. Our ISS studies of $^{92\text{--}100}$Mo, ^{88}Sr, and ^{90}Zr are published in [1]. The calculations for ^{139}La are published in [2]. The figures show the calculations without collisional damping (denoted by ISS) with a constant width $\Gamma = 0.1$ MeV and with collisional damping (denoted by ISS + CD), where the latter were obtained by folding the ISS cross section with the Breit-Wigner distribution in Eq. (6) with an energy-dependent width $\Gamma(E) = 2.5\,(E/15)^2$ MeV. For comparison we display also the QRPA results for the equilibrium deformations, which are denoted by MM, where we use the values in Table II, which were calculated by Möller et al. [11,12] in the framework of their sophisticated micro-macro model. We also show the QRPA results for the average ISS deformations, which are defined as

$$\beta_{\mathrm{ISS}}^2 = \sum_n P(\beta_n, \gamma_n)\beta_n^2, \quad \cos 3\gamma_{\mathrm{ISS}} = \sum_n P(\beta_n, \gamma_n)\cos 3\gamma_n. \tag{24}$$

The corresponding values are listed in Table II as well.

TABLE II. Ground-state deformation parameters for the Kr, Xe, Ba, and Sm isotopes. The equilibrium deformations $\beta_{\mathrm{MM}}, \gamma_{\mathrm{MM}}$ are taken from the compilations [11,12]. The average ISS deformation parameters $\beta_{\mathrm{ISS}}, \gamma_{\mathrm{ISS}}$ are calculated by means of Eq. (24) using the eigenvalues Eq. (13)] and weights Eq. (14)] of the corresponding IBA calculation.

| A	β_{MM}	γ_{MM}	β_{ISS}	γ_{ISS}
		Kr		
78	0.232	60	0.35	26
80	0.062	0	0.26	26
82	0.071	0	0.20	17
84	0.062	0	0.15	20
86	0.053	0	0.14	17
		Ba		
130	0.171	0	0.22	21
132	0.158	20	0.19	28
134	0.132	30	0.16	29
136	0.0	0	0.13	17
138	0.0	0	0.09	17
		Xe		
124	0.208	0	0.21	27
126	0.170	0	0.19	29
128	0.184	25	0.18	29
130	0.158	30	0.17	28
132	0.0	0	0.15	30
134	0.0	0	0.12	17
136	0.0	0	0.12	17
		Sm		
144	0.0	0	0.09	17
146	0.0	0	0.12	28
148	0.161	0	0.14	18
150	0.206	0	0.20	19
152	0.243	0	0.31	4
154	0.270	0	0.34	2
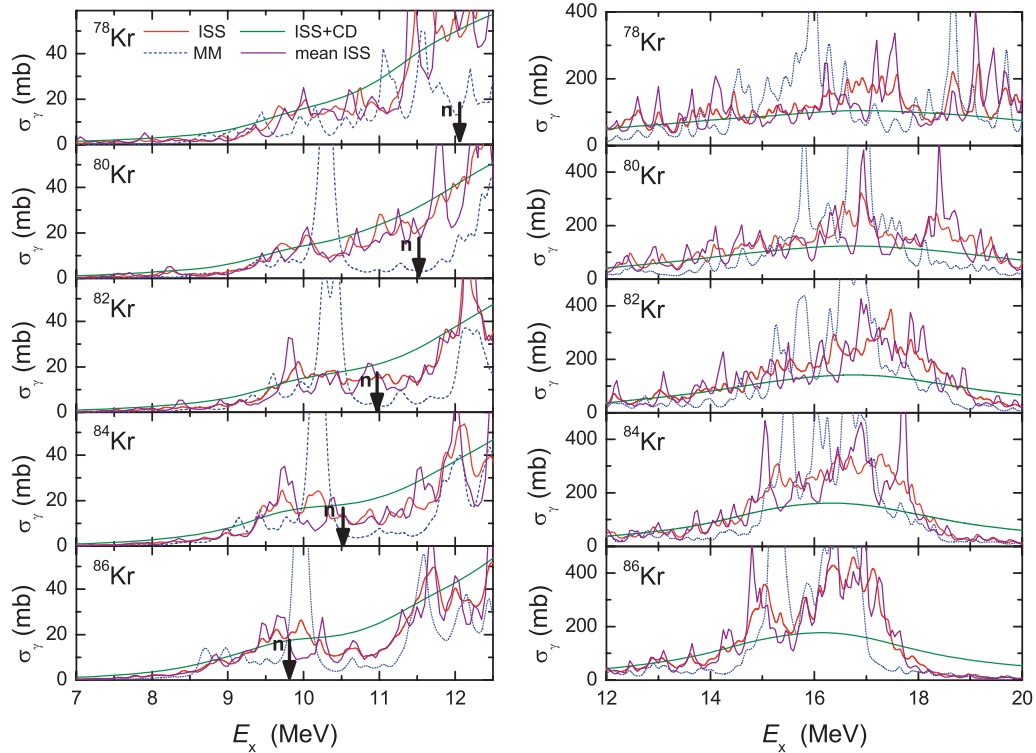
FIG. 5. (Color online) Cross sections for the isotopes $^{78-86}$Kr. Left panel, $E_x = 7–12.5$ MeV; right panel, $E_x = 12–20$ MeV. Red curve (ISS): calculated with ISS-QRPA ($\Gamma = 0.1$ MeV). Dotted blue curve (MM): QRPA ($\Gamma = 0.1$ MeV) with the equilibrium deformations β_{MM}, γ_{MM} in Table II. Green curve (ISS + CD): ISS-QRPA averaged with energy-dependent width $\Gamma(E_x) = 2.5(E_x/15)^2$ MeV. Magenta curve (mean ISS): QRPA ($\Gamma = 0.1$ MeV) with the average ISS deformation parameters β_{ISS}, γ_{ISS} in Table II. The arrows labeled by n mark the position of the neutron-emission threshold of the respective isotope.

In order to characterize the strength function in a more global way we calculated the moments

$$m_k = \int_0^{E_u} dE\, E^k \left[S_{E1}(E) + S_{M1}(E) \right] \tag{25}$$

of our strength functions $S_{E1,M1}(E)$, which are related by Eqs. (1) and (2) to the cross sections shown in Figs. 5–7. The centroid energies $\bar{E}$, the widths $\bar{\gamma}$, and the integrated cross sections Σ presented in Table III are calculated by means of Eq. (25) from the ISS-QRPA results including the collisional damping width $\Gamma(E)$, which are labeled as ISS + CD in the figures. To characterize the low-energy region the energy $E_u = 11$ MeV is considered as an appropriate upper integration limit. Concerning the entire GDR region the moments are calculated using $E_u = 25$ MeV as upper limit. The interval $E = 0–25$ MeV contains more than 85% of the Thomas-Reich-Kuhne (TRK) sum rule. Using the MM-QRPA with collisional damping we also obtained the same quantities for the static equilibrium deformations, which are quoted in Table IV.

Figures 5–7 show that the inclusion of CD (ISS + CD) eliminates the fluctuations of the ISS cross section. However, it barely increases the average cross section in the astrophysically interesting energy range, which was already found in our previous study of the Mo isotopes [1]. Thus the dipole strength in this region results from the Landau fragmentation and the ISS fragmentation, which accounts for the various deformed shapes in the nuclear ground state. The absorption cross

sections calculated for the average ISS deformation parameters β_{ISS} and γ_{ISS} follow the ones for the full ISS calculations, but fluctuate more strongly. This is expected, because the shape fluctuations around the average shape will attenuate the fluctuation of the strength function. Inclusion of CD will make the the results for full ISS and QRPA for β_{ISS} and γ_{ISS} almost identical, which is promising for the QRPA using sophisticated residual interactions.

In all considered chains there is a structural change from spherical to deformed shapes or the reverse. The purely collective models for the GDR predict that an increasing deformation leads to an increasing low-energy dipole cross section, because the GDR splits into two separate peaks [4,6–8,47]. In Ref. [44] the same relation between deformation and low-energy dipole strength was found for the Mo isotopes within the MM + QRPA method based on a Nilsson potential, which was confirmed by ISS-QRPA calculations based on the WS potential [1]. This tendency is also clearly seen for the Sm chain (cf. Fig. 7 and Table III).

According to the equilibrium deformations, the lightest Kr isotope is oblate and all heavier ones have a nearly spherical shape but are expected to be soft against deformation. The IBA parameters show a trend from γ unstable ($\chi = 0$) to spherical ($\zeta = 0$), which is also visible in the deformation distributions in Fig. 3. Although Fig. 5 indicates a certain narrowing of the GDR with increasing A (see the right panel), this is not reflected by a decrease of the low-energy cross
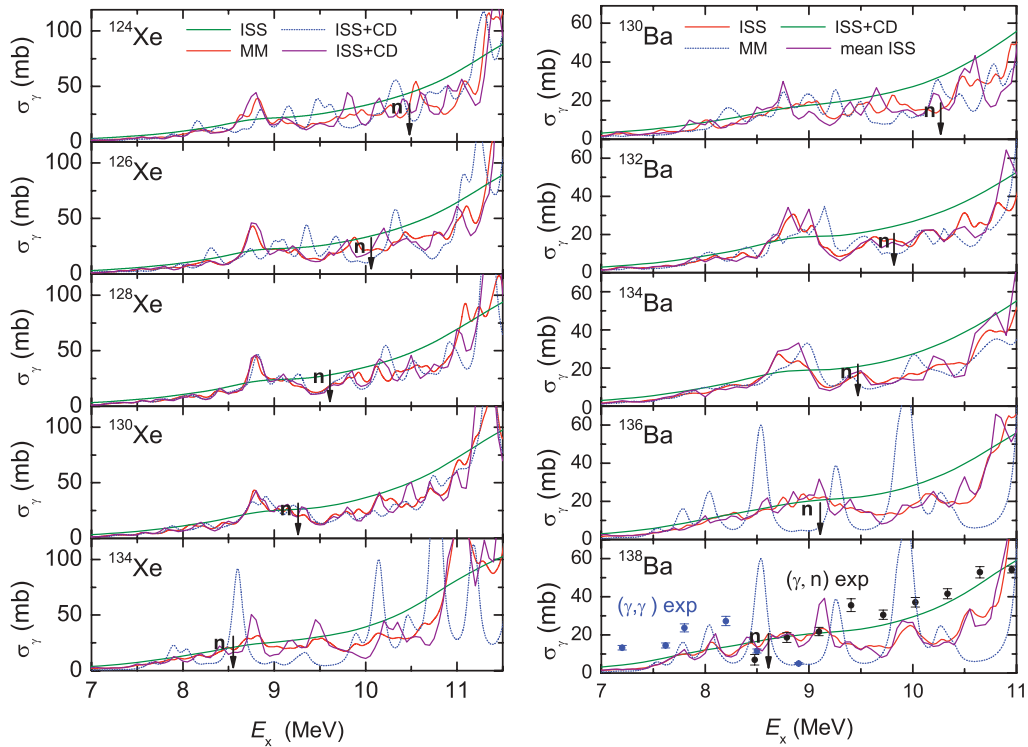
FIG. 6. (Color online) Cross sections for the isotopes $^{124-134}$Xe (left panel) and $^{130-138}$Ba (right panel) in the low-energy region 7–11 MeV. Notations are as in Fig. 5. The arrows labeled by n mark the positions of the neutron-emission threshold of the isotopes. The black dots with error bars in ^{138}Ba display the measured (γ, n) cross section from Ref. [23]. The blue dots below the neutron threshold are (γ, γ') data from the recent measurement by Tonchev *et al.* [50].

section in the left panel and the Σ_{11} values in Table III, which are nearly constant. In fact, the Σ_{11} values for the equilibrium deformation in Table IV increase. There are two mechanisms to explain this unexpected behavior. One is the A dependence of the GDR peak energy, which increases as $A^{-1/3}$ along the isotopic chain. The other can be traced to the emergence of resonances, which reflect the bunching of particle-hole excitations caused by the progressive degeneracy of the single-particle levels with decreasing deformation. The conspicuous example is the strong peak near 10 MeV in the MM calculations, seen in the left panel of Fig. 5, which carries a summed strength of 22 mb MeV for ^{80}Kr and 26 mb MeV for ^{86}Kr. The shape fluctuations in the ISS calculation broaden it progressively with decreasing A, which reflects the increasing probability of deformed shapes. A flat bump remains of the resonance if CD is included.

According to Table II, the Xe and Ba isotopes change from prolate through triaxially deformed to spherical shape with increasing neutron number, i.e., the deformation decreases with increasing mass number A not only in the Kr but also in Ba and Xe isotopes. From macroscopic approaches that take into account the splitting of the GDR into two or three peaks caused by axial or triaxial deformation, one expects that the values of Σ^{11} also decrease [6–8,10]. This trend is not visible. In all cases the values of Σ^{11} increase in the MM calculations. According to the IBA these isotopes tend to γ instability as seen in Fig. 2. ISS also gives an increase of Σ^{11} with A. As for the Kr isotopes, the MM results for Xe and Ba show

strong two-quasiparticle peaks for a spherical shape, which are washed out by the shape fluctuations in the ISS results. Only the Sm chain, which spans the region from spherical to prolate well-deformed nuclei, shows the expected increase of Σ^{11} with A. The examples demonstrate that the incompletely dissolved particle-hole structures can substantially change the absorption cross section near the neutron threshold and can generate an A dependence of the low-energy dipole strength that is opposite to that seen in the macroscopic approaches. Nevertheless, all absorption cross sections, except the ones for semimagic nuclei, smoothly increase with energy.

One notices that for the considered isotopic chains there is only little experimental information. Concerning the γ-absorption cross sections at higher energies, there exist (γ, n) data for the Sm chain and for ^{138}Ba [23] but not for the other nuclides.

The only γ-absorption cross sections for the low-energy region above 5 MeV up to the neutron emission threshold exist for ^{138}Ba from recent experiments with monoenergetic γ rays at the High Intensity Gamma Source facility [50]; these are included in Fig. 6. The data for this $N = 82$ semimagic nucleus show a bump at 8 MeV and possibly another at 9.5 MeV. The $N = 82$ neighbor ^{139}La was studied in [2]. The data show a bump at 7 MeV and a shoulder around 9 MeV, which probably represent the same structures as in ^{138}Ba. The ISS + CD cross section for ^{138}Ba has a shallow shoulder in this region. In case of ^{139}La [2], the ISS + CD cross section has two very
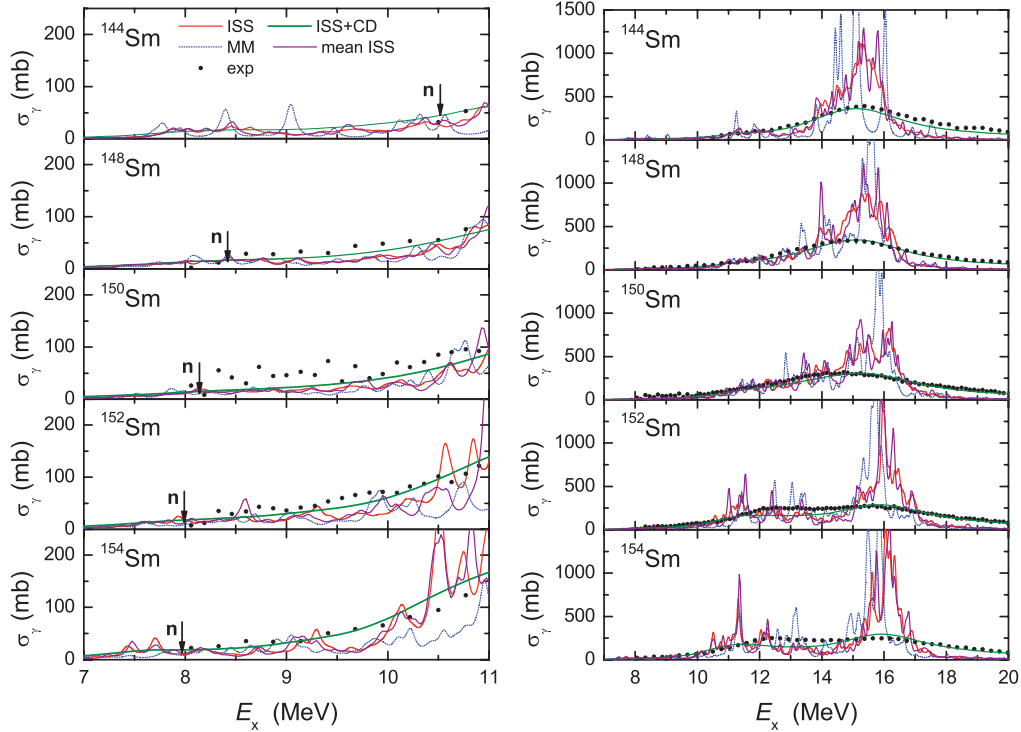
FIG. 7. (Color online) Cross sections for the isotopes $^{144-154}$Sm. Left panel, $E_x = 7$–11 MeV; right panel, $E_x = 7$–20 MeV. Red curves (ISS): calculated with ISS-QRPA ($\Gamma = 0.1$ MeV). Dotted blue curves (MM): QRPA ($\Gamma = 0.1$ MeV) with the equilibrium deformations in Table II. Green line (ISS + CD): QRPA with a energy-dependent width $\Gamma(E_x) = 2.5(E_x/15)^2$ MeV. The black dots are the measured (γ, n) cross sections and the arrows labeled by n mark the position of the neutron-emission threshold of the respective isotope.

broad peaks at 8.5 and 11.5 MeV. Comparing in Fig. 6 the ISS curve with the MM curve (zero deformation), one concludes that the structures originate from spherical two-quasiparticle excitations, which are strongly fragmented due to the shape fluctuations. The deviation of their energies from experimental values may indicate that our choice of the Woods-Saxon potential does not quite correctly reproduce the single-particle levels. A peak in the absorption cross section at 9 MeV was also found in the $N = 50$ semimagic nuclides ^{88}Sr, ^{89}Y, and ^{90}Zr [13–16]. The ISS calculations [1] give a peak at the correct energy, which is also a fragmented spherical two-quasiparticle state. The inclusion of CD broadens the structure somewhat too strongly as compared with the more pronounced "pygmy resonance" seen in experiment. In the case of the $N = 82$ nuclides ^{138}Ba and ^{139}La also, the combination ISS + CD seems to damp the spherical QRPA poles somewhat too strongly. Although the number of studied nuclei is still too small for definite conclusions, one may speculate that the CD width depends more strongly on energy than is assumed. The observation that in many strongly deformed axial nuclei the width of the upper peak of the GDR is twice as big as the width of the lower peak might be taken as evidence for a strong increase in CD with energy. (However, as discussed below, it may be caused by Landau fragmentation as well.) The quadratic energy dependence adopted in this paper is derived from the schematic model of a Fermi gas. A function with a steeper energy dependence would give less CD in the threshold region if its scale is adjusted to reproduce the peak height of

the GDR. Such a reduction of CD would barely reduce the average absorption cross section at these energies (compare the ISS and ISS + CD curves) but give more pronounced pygmy resonances.

In the right panels of Fig. 7, the distance between the two GDR peaks is somewhat overestimated for the well-deformed isotopes ^{152,154}Sm. The discrepancy can be traced to the large values of the deformation parameter β of 0.306 and 0.341, respectively, which reflect the large experimental $B(E2, 2^+ \rightarrow 0^+)$ values [40]. The estimate of the hydrodynamic model $2[E(K = 1) - E(K = 0)]/[E(K = 1) + E(K = 0)] = 0.94\beta$ [4,6–8,47] gives similar splittings of 4.1 and 4.5 MeV, respectively. This indicates some inconsistency between the experimental $B(E2, 2^+ \rightarrow 0^+)$ value and the observed splitting of the GDR. Another problem is visible for the well-deformed isotope ^{154}Sm. In experiment, the second GDR peak has a somewhat smaller height than the first one, whereas in the calculation the result is opposite. Since the high-energy peak is twofold degenerate ($K = \pm 1$), it carries twice the strength of the nondegenerate ($K = 0$) low-energy peak. In order to be lower, its width must be more than twice the width of the first peak. However, collisional damping $\Gamma \propto E_x^2$ gives only $(16/12)^2 = 1.8$. The stronger Landau fragmentation of the low-energy peak exacerbates the discrepancy in the considered case of ^{154}Sm. Many of the well-deformed nuclei behave in the same way: The high-energy peak has the same height as the low-energy one, indicating that its width must be about twice as great [3]. Different versions of the mean

TABLE III. Integral properties derived from the moments m_k of the strength function $S_{E1}(E)$ in Eq. (1) as calculated in the ISS-QRPA with energy-dependent width for the even-A series [78–86]Kr, [130–136]Ba, [124–136]Xe, and [144–154]Sm: $\bar{E} = m_1/m_0$, $\bar{\gamma} = \sqrt{(m_2/m_0) - (m_1/m_0)^2}$, and the integrated cross section $\Sigma = 16\pi^3/(9\hbar c)m_1$. The respective integration limits $E = 11$ and 25 MeV are indicated as an upper index. The percentage of Σ with respect to the TRK sum rule is given in the columns (%).

A	$\bar{E}^{11}$(MeV)	$\bar{\gamma}^{11}$(MeV)	Σ^{11}(MeV mb)	(%)	$\bar{E}^{25}$(MeV)	$\bar{\gamma}^{25}$(MeV)	Σ^{25}(MeV mb)	(%)
			Kr					
78	9.6	1.3	40	3.5	16.3	3.7	991	85
80	9.6	1.3	35	3.0	16.4	3.5	1024	86
82	9.6	1.2	35	2.9	16.4	3.4	1054	87
84	9.6	1.2	39	3.1	16.2	3.3	1095	89
86	9.5	1.2	45	3.6	15.9	3.3	1141	92
			Xe					
124	9.5	1.3	97	5.3	15.8	3.0	1599	87
126	9.5	1.3	98	5.3	15.1	3.3	1725	93
128	9.5	1.3	105	5.6	15.0	3.3	1750	93
130	9.5	1.3	109	5.7	15.0	3.3	1775	94
132	9.5	1.3	113	5.9	14.9	3.3	1806	94
134	9.5	1.3	120	6.2	14.8	3.2	1840	95
			Ba					
130	9.4	1.3	83	4.3	15.6	3.4	1746	91
132	9.4	1.3	82	4.2	15.6	3.3	1766	91
134	9.4	1.3	85	4.3	15.4	3.3	1803	92
136	9.4	1.3	88	4.5	15.4	3.2	1835	93
138	9.4	1.3	93	4.6	15.3	3.2	1866	93
			Sm					
144	9.4	1.3	95	4.5	15.8	2.9	1886	89
146	9.4	1.3	103	4.8	15.7	2.9	1907	89
148	9.4	1.3	110	5.1	15.7	2.9	1921	89
150	9.5	1.3	123	5.6	15.7	3.0	1923	88
152	9.5	1.4	182	8.3	15.7	3.1	1896	86
154	9.5	1.4	223	10.0	15.7	3.1	1892	85

field produce different patterns of Landau fragmentation. In the calculations of Ref. [22] for ^{154}Sm, the Skyrme density functional SLy6 produces stronger Landau fragmentation for the $K = \pm 1$ peak than for the $K = 0$ peak, resulting in a better agreement with experiment, whereas the functionals SkM*, SkI3, and SkT6 give a too high second maximum. For the same nucleus, Ref. [49] obtains sufficient Landau fragmentation in the upper peak for the Skyrme functional SKM*, but not for SLy4 and SkP. The results for ^{154}Sm obtained in [22] and [49] with SkM* disagree. At this point it seems unclear if Landau fragmentation can account for the widths of the two GDR peaks observed in well-deformed axial nuclei.

VII. RANGE OF VALIDITY OF ISS

The coupling between the low-frequency quadrupole mode and the purely collective GDR mode was studied in Ref. [47] by means of the dynamic nuclear collective model (DNCM). The authors find that the dipole strength becomes distributed over several quadrupole excitations. The collisional damping washes out the discrete structures to a smooth envelope. In Ref. [51] the validity of the ISS approximation was investigated in the same model. The discrete spectrum of the DNCM was compared with the continuous strength function obtained by integrating the instantaneous excitation probabilities of the GDR over the probability distribution of

the shape parameters in the ground state, which corresponds to a dense set of sampling points in ISS. The resulting smooth strength function becomes a good approximation of the envelope of the discrete lines if

$$\xi = \frac{d\omega_1}{d\beta}\frac{\beta_0}{\omega_2} \gg 1, \qquad (26)$$

where β_0 is the zero-point amplitude of the quadrupole vibration and ω_1 and ω_2 are the frequencies of the dipole and quadrupole vibrations, respectively. In our previous paper [1], we gave some qualitative estimate that the ISS is applicable to the dipole excitations around the particle emission thresholds according to this condition.

In order to judge the quality of the ISS approximation in this energy region in more detail, we studied the coupling of a single QRPA 1^- pole with the collective quadrupole (2^+) mode in a schematic model. Since the 1^- poles of interest are located substantially away from the peak of the GDR, it suffices for the following discussion to consider them as dressed two-quasiparticle excitations. Accordingly, their energy is not very different from the two-quasiparticle energy, and their transition strength is given by the two-quasiparticle strength times an effective charge accounting for the screening. (A detailed discussion of this approximation is given in [52].) Thus, it is sufficient to use the energies and transition strengths

TABLE IV. Same integral properties as in Table III but here calculated in the QRPA with the equilibrium deformations listed in Table II.

A	$\bar{E}^{11}$(MeV)	$\bar{\gamma}^{11}$(MeV)	Σ^{11}(MeV mb)	(%)	$\bar{E}^{25}$(MeV)	$\bar{\gamma}^{25}$(MeV)	Σ^{25}(MeV mb)	(%)
				Kr				
78	9.6	1.3	29	2.5	16.5	3.4	1000	86
80	9.7	1.1	33	2.8	16.6	3.2	1034	87
82	9.7	1.2	35	2.9	16.5	3.2	1059	87
84	9.6	1.1	40	3.3	16.2	3.2	1098	89
86	9.5	1.1	47	3.8	15.9	3.2	1144	91
				Xe				
124	9.5	1.3	96	5.3	15.2	3.3	1699	92
126	9.5	1.3	96	5.2	15.2	3.3	1728	93
128	9.5	1.3	103	5.6	15.1	3.3	1753	94
130	9.5	1.3	105	5.6	15.0	3.3	1778	94
132	9.5	1.2	105	5.5	15.0	3.2	1807	94
134	9.5	1.2	115	5.9	14.8	3.1	1841	95
				Ba				
130	9.4	1.3	76	4.0	15.6	3.3	1750	92
132	9.4	1.3	78	4.0	15.6	3.3	1771	92
134	9.4	1.3	81	4.2	15.5	3.2	1806	92
136	9.4	1.3	83	4.2	15.5	3.1	1835	93
138	9.4	1.3	90	4.5	15.3	3.1	1866	93
				Sm				
144	9.4	1.3	93	4.4	15.8	2.8	1890	89
146	9.4	1.3	98	4.6	15.8	2.8	1913	89
148	9.4	1.4	108	5.0	15.7	2.9	1923	89
150	9.4	1.4	118	5.4	15.7	3.0	1929	88
152	9.4	1.4	134	6.1	15.6	3.0	1942	88
154	9.4	1.5	151	6.8	15.5	3.0	1957	88

of the two-quasiparticle excitations in the threshold region as a starting point for the following schematic model.

We generated all two-quasiparticle 1^- excitations in the energy interval between 7 and 8 MeV and studied their dependence on deformation. We followed the development in a diabatic way, such that we calculated the overlap of the wave functions of the quasiparticle states at adjacent deformations β_n and β_{n+1} and associated 1^- states by requiring maximal overlap between n and $n + 1$ (cf. [53]). A typical change of the two-quasiparticle energy was found to be 1–3 MeV over the interval $0.1 \leqslant \beta \leqslant 0.3$. One such two-quasiparticle state is selected and its coupling to an axial collective quadrupole degree of freedom is considered, assuming that the coupling is caused by the deformation dependence of the two-quasiparticle energy (as in the DNCM). The quadrupole mode is described by ten equidistant points $\beta_n = 0.04n$, $n = 1, \ldots, 10$ and $\gamma = 0$. The step size is chosen to roughly agree with the distance between the samples in the realistic ISS calculations (cf. Fig. 3). The Hamiltonian for the collective quadrupole motion is given by the matrix

$$H_{n,m}^{(c)} = h(\delta_{n,m+1} - 2\delta_{n,m} + \delta_{n,m-1}) + V(m)\delta_{n,m}. \quad (27)$$

The first term is the discretized kinetic energy where h determines the inertial mass parameter. The second is the discretized potential. We studied the two potentials

$$V_{\text{HO}}(n) = D(n - 7)^2, \quad (28)$$

$$V_{\text{SW}}(n) = \begin{cases} 0 & \text{for} \quad n = 3, \ldots, 8, \\ \infty & \text{for} \quad n = 1, 2, 9, 10, \end{cases} \quad (29)$$

which are the discrete versions of a harmonic oscillator and a square-well potential, respectively. The two-quasiparticle energy is taken as $E^{(2\text{qp})}(n) = [7 + \Delta e(n - 7)]$ MeV with $\Delta e = 0.2$ and 0.6, corresponding to a change of 1 and 3 MeV over the considered deformation range, respectively. The Hamiltonian describing the two-quasiparticle state coupled to the quadrupole mode is

$$H_{n,m}^{(c,2\text{qp})} = H_{n,m}^{(c)} + [7 + \Delta e(n - 7)]\delta_{n,m}. \quad (30)$$

Both $H^{(c)}$ and $H^{(c,2\text{qp})}$ are diagonalized numerically. The resulting eigenvalues are $E^{(c)}(i)$ and $E^{(c,2\text{qp})}(j)$. The resulting eigenvectors are $U_{n,i}^{(c)}$ and $U_{n,j}^{(c,2\text{qp})}$, respectively, where i and j label the respective eigenstates. The transition strength from the ground state 1 to the mixed excited state j at the energy $E^{(c,2\text{qp})}(j)$ is

$$S_{\text{ex}}(j) = \left[\sum_n s(n)U_{n,1}^{(c)}U_{n,j}^{(c,2\text{qp})}\right]^2, \quad (31)$$

where $s(n)$ is the 2qp transition matrix element for deformation point β_n. The analogous ISS strength for the sampling point n is

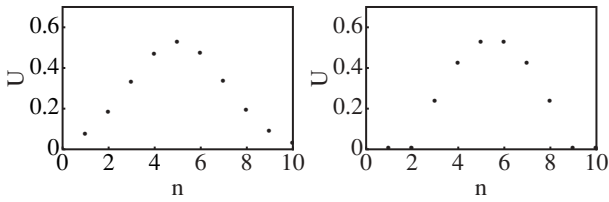$$S_{\text{ISS}}(n) = \left[s(n)U_{n,1}^{(c)}U_{n,1}^{(c)}\right]^2, \quad (32)$$

FIG. 8. Ground-state eigenvectors for the harmonic oscillator (left) and square well (right).

which is associated with the energy $E^{(2\mathrm{qp})}(n)$. Strength functions are generated by folding with a Breit-Wigner distribution in order to account for CD,

$$S_{\mathrm{ex}}(E) = \sum_j S_{\mathrm{ex}}(j) \frac{\Gamma}{2\pi[(E^{(c,2\mathrm{qp})}(j) - E)^2 + (\Gamma/2)^2]}, \quad (33)$$

$$S_{\mathrm{ISS}}(E) = \sum_n S_{\mathrm{ISS}}(n) \frac{\Gamma}{2\pi[(E^{(2\mathrm{qp})}(n) - E)^2 + (\Gamma/2)^2]}. \quad (34)$$

In the following we discuss only the results for $s(n) = 1$, because the study of nonconstant $s(n)$ values, which were derived from the two-quasiparticle excitations in the same way as the two-quasiparticle energies, led to the same conclusions. The choice $h = 1.12$ MeV and $D = 0.028$ MeV gives an excitation energy of $E^{(c)}(2) - E^{(c)}(1) = 0.31$ MeV for the collective quadrupole mode. The corresponding ground-state eigenvectors, shown in Fig. 8, are distributed over five sampling points. Figure 9 compares the exact transition strength (31) with the ISS approximation (32). In the case of the harmonic oscillator potential, the oscillator length is $3\Delta\beta = 0.12$. In the upper panel the two-quasiparticle energy changes by 1 MeV between $\beta = 0.1$ and 0.3 ($n = 3$ and 8, respectively), which corresponds to $\xi = 2$ [cf. Eq. (26)]. As seen, the energies of the coupled states do not agree with the energies of the sampling points. Nevertheless, the locations

and the widths of the distributions are roughly the same. In the lower panels the two-quasiparticle energy changes by 3 MeV between $\beta = 0.1$ and 0.3, which corresponds to $\xi = 6$. Now ISS becomes a rather good approximation to the exact transition strength. This agrees with Ref. [51]. Using the continuous version of ISS, the authors found that for $\xi > 5$ the strong-coupling limit is approached and substantiates the discussion in our previous paper [1]. In the case of the square-well potential, the strong-coupling limit is approached somewhat more slowly. Presumably this reflects the fact that eigenvectors have a lower probability at the turning point than for the harmonic oscillator. At the turning point, the energy equals the potential energy, which is assumed in ISS.

The strength functions take CD into account by folding the transition strengths with a Breit-Wigner distribution. The width $\Gamma = 0.8$ MeV corresponds to the energy-dependent width at 7 MeV, used throughout this paper. In the upper panels of Fig. 9, the energy difference between the sample points is much smaller than the damping width, $\Delta E/\Gamma = 0.2$. All structure is averaged out. ISS and the exact strength function are practically identical. In the lower panels of Fig. 9 the results for $\Delta E/\Gamma = 0.6$ are displayed. Some of the structure survives. In the case of the harmonic oscillator the ISS and exact strength functions nearly agree, because the discrete transition strengths are very similar. In the case of the square-well potential the surviving structures disagree. Since the coupling of the two-quasiparticle state to the collective mode is weaker, the energies and transition strengths of the mixed states disagree with those of the sampling points, and the disagreement is transferred to the strength functions. Hence the fluctuations of the ISS strength function do not represent physical structures. They are just "sampling noise" that should be disregarded. The ISS strength functions for most of the nuclides studied in this paper do barely show structure around the particle emission thresholds, which means that ISS is reliable. The shallow peaks of the ISS + CD strength functions in the Kr isotopes and Sr and Zr isotopes [1] should be considered as real structures (pygmy resonances) predicted by our model, because their width is much larger than the CD damping width.

The number of sampling points is determined by the number of bosons used for diagonalizing the IBA Hamiltonian. In order to study the effects of this coarse graining of the collective mode, we decreased the deformation step in our schematic model to $\Delta\beta = 0.02$. The results for the exact strength functions changed only marginally, which means it is sufficient to restrict the number of bosons to ten. The ISS sampling noise is suppressed on this finer grid. All ISS strength functions become smooth peaks because $\Delta E/\Gamma = 0.3$. The fine structure of the ISS strength function in the left lower panel of Fig. 9 is similar to the exact one, because accidentally we chose the sample points near the deformation points where the mixed states localize. In the case of a spherical nucleus and/or at sufficiently low excitation energy, where CD is weak, one expects to observe the mixed states as resolved lines. Obviously, ISS will not describe these lines individually. Still, the location and the width of the distribution of lines (representing sampling points) will correlate with the location and width of a fragmented QRPA pole.
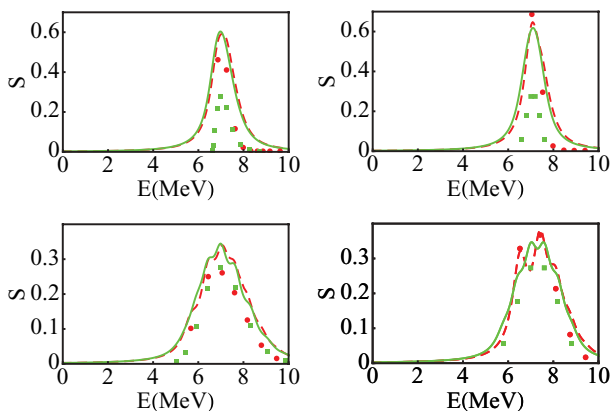

FIG. 9. (Color online) Strength functions of a RPA pole coupled to the collective quadrupole mode. Red circles, exact; red dashed curve, exact + CD ($\Gamma = 0.8$ MeV); green squares, ISS; green curve, ISS + CD ($\Gamma = 0.8$ MeV). Change of the pole energy between $\beta = 0.1$ and 0.3: upper panels, 1 MeV; lower panels, 3 MeV. Potentials: left panels, harmonic oscillator; right panels, square well.

VIII. CONCLUSIONS

The method of instantaneous shape sampling, suggested in our previous Rapid Communication [1] has been presented in extended form. It relies on the assumption that photoexcitation is a fast process as compared to the shape fluctuations of nuclei, such that the total γ-absorption cross section is the sum of the absorption cross sections of a set of instantaneous shapes, each weighted with its probability of being present in the ground state. That is, the γ quantum "takes a snapshot of the instantaneous shape of the nucleus" when it is being absorbed. In the present implementation of the ISS concept, the quadrupole motion is described by the interacting boson approximation and the γ absorption is described by the quasiparticle random phase approximation for a deformed Woods-Saxon potential combined with a dipole-dipole interaction for the $E1$ modes and a spin-spin interaction for the $M1$ modes. The ISS concept can be applied to other versions of the QRPA and a different description of the collective quadrupole mode.

Studying the coupling between a dipole QRPA solution near the particle threshold and the low-lying quadrupole mode in a schematic model, we found that ISS provides a good description of the location and the width of the resulting group of levels, although there is no one-to-one correspondence between the lines. Taking into account the collisional damping by folding the discrete QRPA solutions with a Breit-Wigner function, the resulting ISS + CD strength functions reproduce the exact ones very well, if the distance between the energies of the coupled states is smaller than the damping width.

We applied our version of the ISS-QRPA to the chains of the Kr, Ba, Xe, and Sm isotopes, which all span the transitional regions between deformed and spherical shape. As in our previous study of the Mo isotopes [1], we find that the dipole absorption cross section in the energy region of photonuclear reactions is determined by the Landau fragmentation and the dynamical deformation. In order to reproduce the broad peak of the giant dipole resonance additional CD must be introduced, which we assumed to be proportional to the square of the photon energy. Its scale turned out to be nearly independent of the nuclear mass. CD smoothes out most of the fluctuations of the ISS-QRPA absorption cross section, but it does not increase the cross section in the energy region of photonuclear reactions in any substantial way. For all but semimagic nuclei, the resulting absorption cross section increases with energy in a smooth way, as observed.

Collective hydrodynamic descriptions of the GDR give an increase of the low-energy dipole absorption cross section with nuclear deformation. It is caused by the splitting of the GDR into a low-frequency oscillation along the long and two high-frequency oscillations along the short axes. In the case of the Mo and Sm isotopic chains, the deformation increases with neutron number. The ISS-QRPA reproduces the expected increase of the low-energy dipole absorption cross section. However, in the cases of the Kr, Ba, and Xe chains, for which the deformation decreases with increasing neutron number, the expected decrease of the low-energy cross section is not found. The ISS-QRPA predicts a nearly constant value of the cumulative low-energy cross section ($E_x \leqslant 11$ MeV) when the shell closure is approached. The reason is the the $A^{-1/3}$ decrease of the GDR peak energy as well as the progressive bunching of the two-quasiparticle excitations when approaching spherical shape.

In the case of semimagic nuclei, relicts of these bunches survive the damping by shape fluctuations and collisional damping. They appear as broad bumps in the ISS-QRPA cross section, which may substantially enhance the absorption cross section around the particle thresholds. These pygmy resonances are two-quasiparticle excitations dressed with isovector dipole vibrations and fragmented by coupling to shape fluctuations. In the case of the $N = 50$ isotones, the position of the resonance is well reproduced. In the case of the $N = 82$ isotones, some discrepancy between the calculated and observed locations may point to inaccuracies of the single-particle levels of the adopted Woods-Saxon potential.

[1] S. Q. Zhang, I. Bentley, S. Brant, F. Dönau, S. Frauendorf, B. Kämpfer, R. Schwengner, and A. Wagner, Phys. Rev. C **80**, 021307(R) (2009).

[2] A. Makinaga *et al.*, Phys. Rev. C **82**, 024314 (2010).

[3] S. S. Dietrich and B. L. Berman, At. Data Nucl. Data Tables **38**, 199 (1988).

[4] A. Bohr and B. Mottelson, *Nuclear Structure* (Benjamin, New York, 1975), Vol. II, pp. 475 ff.

[5] S. G. Kadmenskii *et al.*, Sov. J. Nucl. Phys. **37**, 165 (1983).

[6] K. Okomoto, Phys. Rev. **110**, 143 (1958).

[7] M. Danos, Nucl. Phys. **5**, 23 (1958).

[8] A. R. Junghans, G. Rusev, R. Schwengner, A. Wagner, and E. Grosse, Phys. Lett. B **670**, 200 (2008).

[9] T. Rauscher and F.-K. Thielemann, At. Data Nucl. Data Tables **75**, 1 (2000).

[10] F.-K. Thielemann and M. Arnould, in *Proceedings of the International Conference on Nuclear Data for Science and Technology*, edited by K. Blöckhoff (Reidel, Dordrecht, 1983), p. 762.

[11] P. Möller, R. J. Nix, W. D. Myers, and W. J. Swiatecki, At. Data Nucl. Data Tables **59**, 185 (1995).

[12] P. Möller, R. Bengtsson, B. G. Carlsson, P. Olivius, T. Ichikawa, H. Sagawa, and A. Iwamoto, At. Data Nucl. Data Tables **94**, 758 (2008).

[13] R. Schwengner *et al.*, Phys. Rev. C **76**, 034321 (2007).

[14] G. Rusev *et al.*, Phys. Rev. C **77**, 064321 (2008).

[15] R. Schwengner *et al.*, Phys. Rev. C **78**, 064314 (2008).

[16] N. Benouaret *et al.*, Phys. Rev. C **79**, 014303 (2009).

[17] G. Rusev *et al.*, Phys. Rev. C **79**, 061302(R) (2009).

[18] D. J. Rowe, *Nuclear Collective Motion* (Methuen, London, 1970).

[19] P. Ring and P. Schuck, *The Nuclear Many Body Problem* (Springer, New York, 1980).

[20] V. G. Soloviev, *Theory of Atomic Nuclei: Quasiparticles and Phonons* (Institute of Physics, Bristol, 1992).

[21] N. Paar, D. Vretenar, E. Khan, and G. Colo, Rep. Prog. Phys. **70**, 691 (2007).

[22] V. O. Nesterenko, W. Kleinig, J. Kvasil, P. Vesely, P.-G. Reinhard, and D. S. Dolci, Phys. Rev. C **74**, 064306 (2006).

[23] [http://www-nds.iaea.org/RIPL-2/].

[24] S. Goriely and E. Khan, Nucl. Phys. A **706**, 217 (2002).

[25] G. F. Bertsch *et al.*, Rev. Mod. Phys. **55**, 287 (1983).

[26] J. Wambach, Rep. Prog. Phys. **51**, 989 (1988).

[27] N. Tsoneva and H. Lenske, J. Phys. G **35**, 014047 (2008).

[28] N. Tsoneva and H. Lenske, Phys. Rev. C **77**, 024321 (2008).

[29] D. Sarchi *et al.*, Phys. Lett. B **601**, 27, (2004); **601**, 054318 (2007).

[30] E. Litvinova, P. Ring, and V. Tselyaev, Phys. Rev. C **78**, 014312 (2008).

[31] E. V. Litvinova and V. I. Tselyaev, Phys. Rev. C **75**, 054318 (2007).

[32] E. Litvinova, P. Ring, and V. Tselyaev, Phys. Rev. C **75**, 064308 (2007).

[33] E. Litvinova, P. Ring, V. Tselyaev, and K. Langanke, Phys. Rev. C **79**, 054312 (2009).

[34] E. Litvinova, H. P. Loens, K. Langanke, G. Martinez-Pinedo, T. Rauscher, P. Ring, F.-K. Thielemann, and V. Tselyaev, Nucl. Phys. A **823**, 26 (2009).

[35] F. Iachello and A. Arima, *The Interacting Boson Model* (Cambridge University Press, Cambridge, 1987).

[36] R. Casten, Prog. Part. Nucl. Phys. **62**, 183 (2009).

[37] E. A. McCutchan, N. V. Zamfir, and R. F. Casten, Phys. Rev. C **69**, 064306 (2004).

[38] D. Tonev *et al.*, Phys. Rev. C **76**, 044313 (2007).

[39] V. Werner, N. Pietralla, P. vonBrentano, R. F. Casten, and R. V. Jolos, Phys. Rev. C **61**, 021301(R) (2000).

[40] S. Raman, C. W. Nestor Jr., and P. Tikkanen, At. Data Nucl. Data Tables **78**, 1 (2001).

[41] S. Kahane, S. Raman, and J. Dudek, Phys. Rev. C **40**, 2282 (1989).

[42] H. Sakamoto and T. Kishimoto, Nucl. Phys. A **501**, 205 (1989).

[43] V. O. Nesterenko, J. Kvasil, and P.-G. Reinhard, Phys. Rev. C **66**, 044307 (2002).

[44] F. Donau, G. Rusev, R. Schwengner, A. R. Junghans, K. D. Schilling, and A. Wagner, Phys. Rev. C **76**, 014317 (2007).

[45] G. Rusev *et al.*, Phys. Rev. C **73**, 044308 (2006).

[46] D. Frekers *et al.*, Phys. Lett. B **244**, 178 (1990).

[47] M. Danos and W. Greiner, Phys. Rev. **134**, B284 (1964).

[48] W. Kleinig, V. O. Nesterenko, J. Kvasil, P.-G. Reinhard, and P. Vesely, Phys. Rev. C **78**, 044313 (2008).

[49] K. Yoshida and T. Nakatsukasa, arXiv:1008.1520 [nucl-th].

[50] A. P. Tonchev, S. L. Hammond, J. H. Kelley, E. Kwan, H. Lenske, G. Rusev, W. Tornow, and N. Tsoneva, Phys. Rev. Lett. **104**, 072501 (2010).

[51] J. Le Tourneux, Mat. Fys. Medd. K. Dan. Vidensk. Selsk. **34**, 11 (1965); cf. A. Bohr and B. Mottelson, *Nuclear Structure* (Ref. [4]), Vol. II, pp. 455 ff.

[52] A. Bohr and B. Mottelson, *Nuclear Structure* (Ref. [4]), Vol. II, pp.

[53] S. Frauendorf, Nucl. Phys. A **667**, 115 (2000).